Examining the Potential Impact of SWOT Observations in an Ocean Analysis–Forecasting System[a]

MATTHEW J. CARRIER, HANS E. NGODOCK, AND SCOTT R. SMITH

Naval Research Laboratory, Stennis Space Center, Mississippi

INNOCENT SOUOPGUI

Department of Marine Sciences, University of Southern Mississippi, Stennis Space Center, Mississippi

BRENT BARTELS

Vencore, Inc., Chantilly, Virginia

(Manuscript received 15 October 2015, in final form 7 June 2016)

ABSTRACT

NASA's Surface Water and Ocean Topography (SWOT) satellite, scheduled for launch in 2020, will provide observations of sea surface height anomaly (SSHA) at a significantly higher spatial resolution than current satellite altimeters. This new observation type is expected to improve the ocean model mesoscale circulation. The potential improvement that SWOT will provide is investigated in this work by way of twin-data assimilation experiments using the Navy Coastal Ocean Model four-dimensional variational data assimilation (NCOM-4DVAR) system in its weak constraint formulation. Simulated SWOT observations are sampled from an ocean model run (referred to as the ''nature'' run) using an observation-simulator program provided by the SWOT science team. The SWOT simulator provides realistic spatial coverage, resolution, and noise characteristics based on the expected performance of the actual satellite. Twin-data assimilation experiments are run for a two-month period during which simulated observations are assimilated into a separate model (known as the background model) in a series of 96-h windows. The final condition of each analysis window is used to initialize a new 96-h forecast, and each forecast is compared to the nature run to determine the impact of the assimilated data. It is demonstrated here that the simulated SWOT observations help to constrain the model mesoscale to be more consistent with the nature run than the assimilation of traditional altimeter observations alone. The findings of this study suggest that data from SWOT may have a substantial impact on improving the ocean model forecast of mesoscale features and surface ocean velocity.

1. Introduction

Accurate sea surface height (SSH) prediction is a major component of ocean modeling in global to regional domains. Within these domains, the surface ocean transport is dominated by mesoscale features in the sea surface, which are primarily constrained in ocean modeling by the assimilation of satellite altimetry data. Conventional satellite altimeters, such as the *Jason* series and AltiKa (Lillibridge et al. 2014), have high resolution in the along-track direction, but have no resolution in the cross-track direction. Only by gathering multiple altimeter tracks from all available satellites over a certain time interval can more information be gained. However, even by combining the observations from two altimeters in a particular region, the combined cross-track resolution of all available altimeter tracks is still limited to 150 km (Fu and Ubelmann 2014). This makes it very difficult to properly constrain the model mesoscale for current-generation ocean models, which routinely have horizontal resolutions of less than 10 km. The work of Carrier et al. (2016) demonstrate the impact of coarse altimeter resolution in a 6-km Navy Coastal Ocean Model (NCOM) Gulf of Mexico experiment.

[a] Naval Research Laboratory Contribution Number NRL/JA/7320-15-2822.

Corresponding author address: Matthew J. Carrier, Naval Research Laboratory, Bldg. 1009, Balch Blvd., Stennis Space Center, MS 39529.
E-mail: matthew.carrier@nrlssc.navy.mil

DOI: 10.1175/MWR-D-15-0361.1

This work, based on a dense surface drifter deployment in the summer of 2012, sought to investigate the impact of ocean velocity observations on the ocean model sea surface height field; comparisons are made to conventional assimilation of altimeter observations. It is shown that the assimilation of altimeter data alone is insufficient in constraining the primary Loop Current eddy with enough accuracy to properly simulate drifter trajectories. When the surface velocity observations are added, however, the model properly constrains the shape of the primary Loop Current eddy and the modeled drifter trajectories are also improved. It is theorized by Carrier et al. (2016) that the lack of altimeter data in the cross-track direction is primarily responsible for this problem, whereas the high-spatial resolution of the drifter observations was able to resolve the mesoscale features. It should be noted, though, that the drifter observations used in this experiment were from a unique dataset and that these types of observations are not readily available.

A future satellite altimeter, NASA's Surface Water and Ocean Topography (SWOT), is expected to provide high-resolution altimetry observations in both the along- and cross-track directions. Conventional satellite altimeters are radar based and provide observations at the satellite nadir along the satellite orbit path. SWOT differs from these traditional altimeters in that it is based on radar interferometry that allows for observation collection along a wider swath than the nadir path alone (Fu and Ubelmann 2014). SWOT will provide sea surface height anomaly SSHA observations across a 120-km swath at 2-km resolution and will cover over 90% of the globe at least once every 21 days. With this type of data, it is expected that SWOT will provide ocean models the necessary observational resolution to properly constrain the mesoscale to submesoscale structures in the global ocean surface.

There has been some recent work in attempting to assess the potential impact of SWOT observations in generating two-dimensional maps of SSH, such as those obtained from Archiving, Validation, and Interpretation of Satellite Oceanographic Data (AVISO; produced by Ssalto/Duacs and distributed by AVISO, with support from CNES at http://www.aviso.altimetry.fr/en/home.html). Ubelmann et al. (2015) employ a ''dynamic interpolation'' of simulated SWOT observations that is based on the conservation of potential vorticity. This study found that for temporal gaps shorter than 20 days, the interpolation performed well in reconstructing the evolution of eddies smaller than 100 km. Another effort, Pujol et al. (2012), employs an ocean system simulation experiment, in an attempt to determine the observational capability of the SWOT instrument and its potential use in creating high-quality mesoscale sea level anomaly (SLA) fields by way of optimal interpolation (OI). Pujol et al. (2012) determined that a SWOT instrument can provide as much information as four traditional altimeters when used in reconstructing surface mesoscale fields. They also found that combining observations from SWOT and the other traditional altimeters produces a better result than either instrument type alone.

This present effort advances the work started by others by utilizing simulated SWOT observations in a realistic analysis and forecasting system. The goal here is to assess whether SWOT observations will be capable of constraining the model sea surface height and velocity structures at the mesoscale (50–250 km). In this case, the regional NCOM and its advanced four-dimensional variational data analysis component (NCOM-4DVAR) are used to assimilate simulated SWOT observations in a series of twin-data assimilation experiments to examine the impact on the model forecast. Multiple experiments are run: 1) analysis–forecast using simulated observations from conventional altimeters, 2) analysis–forecast using simulated SWOT observations, and 3) analysis–forecast using observations from a combination of conventional altimeters and SWOT. A model free run (i.e., no assimilation) is also provided for reference. This methodology can be viewed as an observing system simulation experiment (OSSE). OSSEs are commonly used to investigate the potential impact of a new observing and/or a new data assimilation system. OSSEs rely on simulating observations (usually by sampling from a dynamical model of the atmosphere or ocean, i.e., the nature run) and assimilating these observations into a separate model run (usually some perturbation of the nature run). In doing so, the impact of assimilating or withholding certain observations or observation types can be thoroughly investigated. One example of a truly robust OSSE is demonstrated in the Gulf of Mexico by Halliwell et al. (2014). This provides the first example of an ocean OSSE that employs more rigorous criteria, which had previously been adopted for atmospheric analysis–forecast systems. This includes simulating the real ocean (i.e., the nature run) using a different model than what is used to generate the model background forecast, and generating observations from the nature run by adding realistic errors based on known or estimated characteristics. This present work does not go to these lengths, as the nature run and model forecast use the same ocean model. However, this present study provides insight and useful indications as to the potential impact of the new altimetry data provided by SWOT.

This paper is organized as follows: section 2 provides an overview of the ocean model and analysis system,

section 3 provides a description of the nature and background model runs as well as the method of simulating the observations, section 4 introduces the twin-data assimilation experiments and reviews the results while offering conclusions based on their findings, and section 5 then offers a summary of the major findings.

2. Ocean model and analysis system

a. Navy Coastal Ocean Model and selected regional domain

The ocean model selected for this work and the regional domain configuration match that of Carrier et al. (2016), the description from that article follows in the next two paragraphs. The dynamical model used for this work is NCOM, which is a primitive equation ocean model using the hydrostatic and Boussinesq approximations, with a free surface and a generalized vertical coordinate that can be configured with terrain-following free sigma or fixed sigma, or constant z-level surfaces in a number of combinations (Barron et al. 2006). The model employs the Mellor–Yamada level-2.5 turbulence closure parameterization (Mellor and Yamada 1982) for vertical diffusion and the Smagorinsky scheme (Smagorinsky 1963) for horizontal diffusion.

The model domain for all three experiments is the Gulf of Mexico, which in this case extends from 18°–31°N to 79°–98°W using a spherical coordinate projection at a horizontal resolution of 6 km. The model has 50 layers in the vertical extending down to a maximum of 5500 m. Lateral boundary conditions for each experiment are provided by the global Hybrid Coordinate Ocean Model (HYCOM; Bleck 2002) at $1/12^\circ$ resolution, as is the model initial condition on 1 April 2014. Global HYCOM is an operational assimilative model, using the three-dimensional variational (3DVAR) Navy Coupled Ocean Data Assimilation (NCODA) system (Cummings and Smedstad 2013). Surface atmospheric forcing, such as wind stress, atmospheric pressure, and surface heat flux is provided by the Navy Global Environmental Model (NAVGEM), a spectral model with a horizontal resolution of roughly 37 km with 50 vertical levels (https://hycom.org/dataserver/navgem). River forcing is provided via an internal NRL river product that includes monthly mean river data for each major river across the globe. There is no tidal forcing added to the boundary conditions for these experiments.

b. Ocean analysis system

The data assimilation system selected here has been described within numerous works (i.e., Ngodock and Carrier 2013, 2014; Carrier et al. 2014, 2016). The following description over the next two paragraphs is from Carrier et al. (2016) and is repeated here for completeness. The NCOM-4DVAR is a variational assimilation system based on the indirect representer method as described by Bennett (1992, 2002) and Chua and Bennett (2001). The representer method aims to find an optimal analysis solution as the linear combination of a first guess (i.e., prior model solution) and a finite number of representer functions, one per datum:

$$\hat{u}(x,t) = u_F(x,t) + \sum_{m=1}^{M} \hat{\beta}_m r_m(x,t), \tag{1}$$

where $\hat{u}(x, t)$ is the optimal analysis solution, $u_F(x, t)$ is the prior forecast, $r_m(x, t)$ is the representer function for the mth observation, and $\hat{\beta}_m$ is the mth representer coefficient. A representer function is the model response to an impulse forcing over the entire time–space domain. The impulse forcing is the innovation calculated as the difference between the background model forecast and a single observation (at the location of the observation). The representer coefficients can be found by solving the linear system:

$$(\mathbf{R} + \mathbf{O})\beta = \mathbf{y} - \mathbf{H}\mathbf{x}^f, \tag{2}$$

where $\mathbf{O}$ is the observation error covariance, $\mathbf{y}$ is the observation vector, $\mathbf{H}$ is the linear observation operator that maps the model fields to the observation locations, $\mathbf{x}^f$ is the model vector, and $\mathbf{R}$ is the representer matrix and is equivalent to $\mathbf{HMBM}^{\mathrm{T}}\mathbf{H}^{\mathrm{T}}$ ($\mathbf{M}$ is the tangent linear model; $\mathbf{M}^{\mathrm{T}}$ is the adjoint model; $\mathbf{B}$ is the initial or model error covariance, depending on what portion of the $\mathbf{y} - \mathbf{H}\mathbf{x}^f$ vector it is applied to; and the superscript T denotes the linear transposition). Since the matrix $\mathbf{R} + \mathbf{O}$ is symmetric and positive definite (Bennett, 2002), Eq. (2) can be solved for β iteratively using a linear solver, such as the conjugate gradient method. From Eq. (2) it is clear that the $\hat{\beta}_m$ for each representer can be found by integrating the adjoint and tangent linear (TL) models over some number of minimization steps until convergence. Once found, $\hat{\beta}_m$ is acted upon in Eq. (1), involving one final application of the adjoint and TL models to find the analysis increment.

The background and model error covariance in NCOM-4DVAR follow the work of Weaver and Courtier (2001) and Carrier and Ngodock (2010), where the error correlation portion of the covariance, for both the model and the initial condition errors, are not directly calculated and stored in NCOM-4DVAR; rather, the *effect* of the correlation matrix acting on an input vector is modeled by the solution of a diffusion equation. For a description of the implementation of this method

in NCOM-4DVAR, we refer the reader to Carrier and Ngodock (2010).

3. Model simulations and observation sampling

a. Nature and background model simulations

Twin-data assimilation experiments, also referred to as OSSEs, are a useful tool in evaluating a new data assimilation system, a new observing system, or both. It does not require real observations and it allows for the flexibility of selecting observation types and locations that can significantly vary from one experiment to another and for testing all the components of the data assimilation system itself. A twin-data assimilation experiment also provides the entire ''true'' state of the environment, this is in contrast to reality where an estimate of the true state is only given at the observation locations. This allows for the possibility of examining the analysis and forecast state at locations far from observations. In this work, the SWOT satellite is not yet operational; therefore, a twin-data assimilation experiment is the only current method available to assess the potential impact of SWOT observations on the ocean model.

To test the simulated SWOT data, the ocean model described in the previous section is run three times: once to create a ''nature run,'' which is considered the ''truth,'' and again to create the background model run, which has error added to it. In this case the ''error'' takes the form of a perturbed initial condition; the resulting model simulation follows a different trajectory than the nature run. Observations are sampled from the nature run and are assimilated into the background to create a third model run, known as the assimilative model. If the observations are useful and provide pertinent information regarding the environment, the assimilative model should, over time, approach the nature run solution in a root-mean-square error sense.

The Gulf of Mexico (GoM) is a useful domain for a study such as the one presented here. The region is dominated by a strong current, known as the Loop Current (LC), which enters the GoM from the south through the Yucatan Channel and exits through the Straits of Florida to the east. This current can extend far into the northeastern GoM. The extent of this penetration varies from a position known as ''port to port,'' where the current travels almost directly from the Yucatan Channel to the Straits of Florida, to an extended position northward of 26°N (average extension), and sometimes as far north as 28°N (fully extended; Leben 2005). When the LC reaches its ''fully extended'' position an eddy can form and pinch-off from the larger LC flow; this is known as a Loop Current Eddy (LCE). After the LCE detaches from the LC, the LC normally returns to its port-to-port position as the LCE migrates westward across the GoM at a speed of roughly 2–5 km day^{-1}. Unlike larger western boundary currents, which exhibit multiple meanders and eddies, the GoM LC regime normally only exhibits one or two LCEs at a time. This allows for a simpler investigation of the impact of data assimilation on the model representation of the surface ocean topography, which is ideal for this current study.

The nature run covers a 68-day period from 1 April to 4 June 2014. The background run is created as a perturbation from the nature run by offsetting its initial condition by 24 days. In other words, the background run is generated by taking the ocean model state from the nature run on 25 April 2014 and using it as the initial condition for 1 April 2014. The forcing and boundary conditions are the same between the nature and background runs. Because of the nonlinearity of the Loop Current circulation in the Gulf of Mexico, especially during a LCE shedding event, the difference in the initial condition of the two model runs should result in a substantially different model trajectory, without the need of perturbing the surface or lateral boundary conditions in the model. Separating the nature and background runs by only 24 days ensures that the background run does not deviate too far from the true state; thus, enabling the variational assimilation system to maintain efficiency.

For a study such as this that relies on an ocean forecast model to produce simulated observations, it is important to verify that the model is capable of simulating physically realistic features that the observing system is expected to capture. In the case of this present work, NCOM is relied upon to produce a realistic ocean state. This is a safe assumption to make, as NCOM was, until 5 April 2013, the operational global ocean model used by the U.S. Navy and as such has undergone extensive internal evaluation (Barron et al. 2007). In addition to this, NCOM is currently the operational regional ocean forecast model used by the U.S. Navy (Martin et al. 2009). NCOM has also been examined extensively in peer-reviewed literature. Barron et al. (2004) examined the global model's predictive capability in terms of the SSH forecast. For regional applications, specifically within the Gulf of Mexico region, NCOM has been used to perform current estimation in a multimodel ensemble Kalman filter (Coelho et al. 2015) and by Jacobs et al. (2014) to investigate the underlying assumptions in the data assimilation methodology used in the analysis step. Finally, there have been several studies that have employed the specific 6-km Gulf of Mexico configuration of NCOM used in this present study. Carrier et al. (2014)

used this configuration to examine the impact of drifter-derived surface velocity observations on the NCOM forecast of surface currents; these results were favorably compared to real observations. Muscarella et al. (2015) also used this configuration to examine Lagrangian predictability when performing surface velocity assimilation; the results here were also compared favorably to available observations. Finally, this configuration of NCOM was used in the previously mentioned study by Carrier et al. (2016) to examine the impact of surface velocity observations on the sea surface height.

In this present work, the nature run can be examined through the use of several metrics: the transport through a cross section of the Yucatan Channel and the Florida Straits, the average flow speeds of the LC and swirl speed of the LCE, and the average daily progression of the LCE as it moves westward through the Gulf. According to Schlitz (1973), the average transport through the Yucatan Channel is 23 to 33 Sv (1 Sv $\equiv 10^6\,m^3\,s^{-1}$), whereas more recent studies, such as Ochoa et al. (2001), suggest that the value is closer to 20–31 Sv. From 1 April to 4 June 2014, the average transport through the Yucatan Channel from the nature run is 31.57 Sv. Likewise, the average transport through the Florida Straits is similar at 30.96 Sv. According to Oey et al. (2005), the average flow speed for the LC ranges from 1.5 to 1.8 m s^{-1}. During this present experiment, the average flow speed for the LC is computed to be 1.65 m s^{-1}. Cooper et al. (1990) compute the average LCE swirl speed to be 1.8–2.0 m s^{-1}. In this study, the LCE has an average swirl speed of 1.8 m s^{-1}. The LCE is known to progress westward at about 2–5 km day^{-1}; in this present experiment, the LCE progresses westward at an average speed of 3.06 km day^{-1}. The transport, LC flow speed, the LCE swirl speed, and the LCE progression are all within the expected values.

One can also examine the SSH wavenumber spectrum to ascertain the slope of the spectrum in the mesoscale band (50–250 km). According to Le Traon et al. (2008), Sasaki and Klein (2012), Richman et al. (2012), and others, the expected slope of the SSH wavenumber spectrum within the mesoscale band should vary as $k^{-11/3}$, where k is the wavenumber. Figure 1 shows the directionally averaged SSH wavenumber spectrum computed from each 3-hourly output from the nature run NCOM model over the course of the experiment time period. Also shown in this figure are lines indicating the $k^{-11/3}$ (blue dashed) and $k^{-5/3}$ (green dashed) slopes. Figure 1 indicates that the spectral slope within the mesoscale band is steeper than $k^{-5/3}$ and flatter than $k^{-11/3}$, but is still close to expected values. The previous studies with the NCOM model, the validation of the model prior to operational use, the studies that use this particular 6-km GoM model, as well as the examination of the nature run here, indicate that the model is capable of representing realistic ocean features and phenomenon at the scales (i.e., mesoscale) to be investigated in this present study.

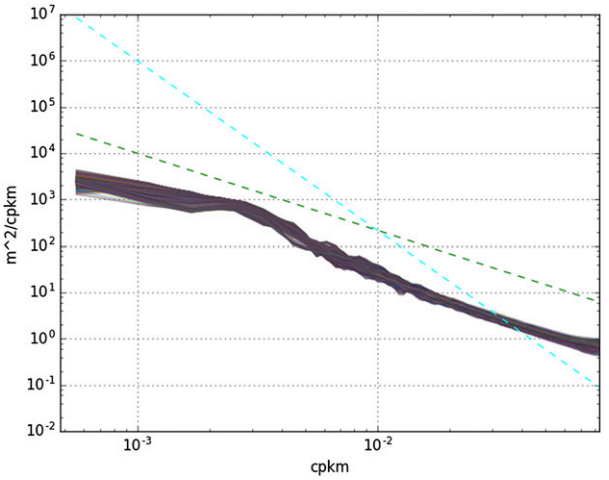

FIG. 1. Directionally averaged SSH wavenumber spectrum (spectrum indicated on y axis, wavenumber on x axis) from each 3-hourly output of the NCOM nature run over the time frame of the experiment (1 Apr–4 Jun 2014). Line with a $k^{-5/3}$ slope is the green dashed line; line with a $k^{-11/3}$ slope is the blue dashed line.

It is necessary to examine the differences in the nature and background model runs in order to identify those features that may be corrected by the assimilation of observations. Figure 2 shows the evolution of the LCE in the nature and background runs at three separate times. Figure 2a shows the nature run initial condition as compared to the background run initial condition in Fig. 2b at 1 April 2014. In both the nature and the background model runs, the LC is in the process of forming an eddy; in the nature run this process is in the fully extended stage of the Loop Current, where the central eddy (located at 25°N, 86°W) is still attached to the LC itself. In the background run, the LCE has just about pinched off from the LC and there is a fairly strong Loop Current frontal eddy (LCFE) located at 24°N, 84°W. Figures 2c and 2d show the nature run and the background run at 1 May 2014, respectively. At this time the nature run has the primary LCE still slightly attached to the Loop Current, whereas the background run has the LCE full detached. Also, the LCE in the nature run is slightly elongated in the north–south direction, which differs from the background run that is elongated in the northwest–southeast direction. Near the end of the experiment, 1 June 2014, the nature run (Fig. 2e) and the background run (Fig. 2f) both show the LCE detached from the Loop Current and slowly propagating westward. The nature run LCE, now

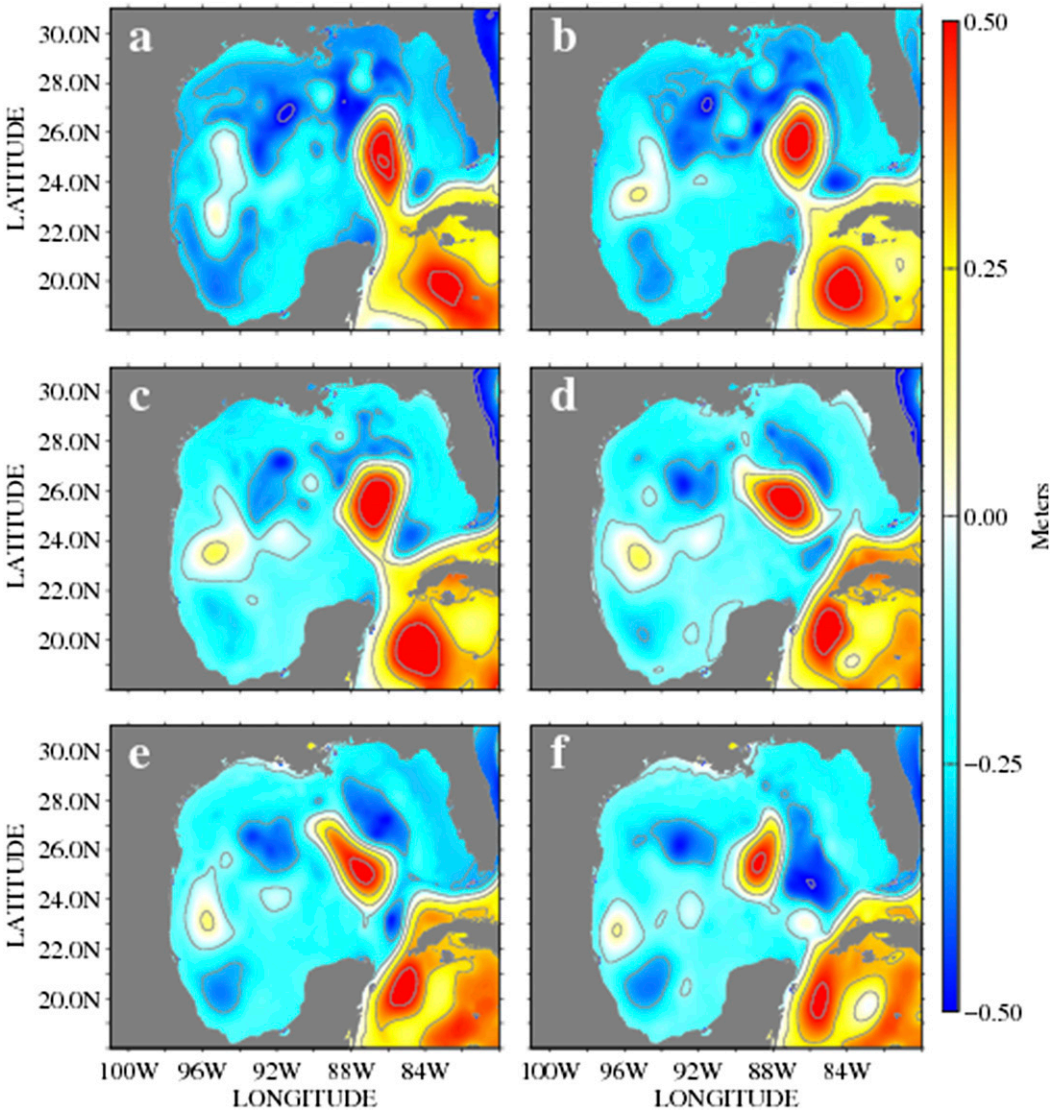

FIG. 2. Model-simulated SSH (m) for nature run, valid at (a) 1 Apr 2014, (c) 1 May 2014, and (e) 1 Jun 2014. (d)–(f) As in (a)–(c), but for the background run.

centered near 25°N, 87°W, is slightly elongated in the northwest–southeast direction and is slightly east of the background run LCE, centered near 25.5°N, 89°W. By 1 June the background model runs exhibit a large cyclonic eddy to the southeast of the LCE. The nature run does not exhibit the same pattern as the background model; instead, the nature run shows one large cyclonic eddy to the northeast of the primary LCE, with a smaller cyclonic eddy to the south of the LCE.

b. Observation sampling

To assess the impact of observations via a twin-data assimilation experiment, it is important to sample the nature run at both spatial and temporal frequencies that are realistic for ocean observing systems. For the experiments shown here, simulated observations of surface and subsurface temperature and salinity are generated, as well as observations of sea surface height from conventional altimeters as well as from SWOT. For the conventional observations, the spatial and temporal sampling is designed by first processing actual ocean observations through the operational NCODA data preparation utility for the time period covering 5 April–4 June 2014. Data processing begins four days past the model initial condition time to allow for model spinup in the background simulation. Both remotely sensed and in situ ocean observation data are processed from GOES-East sea surface temperatures (SST), Argo

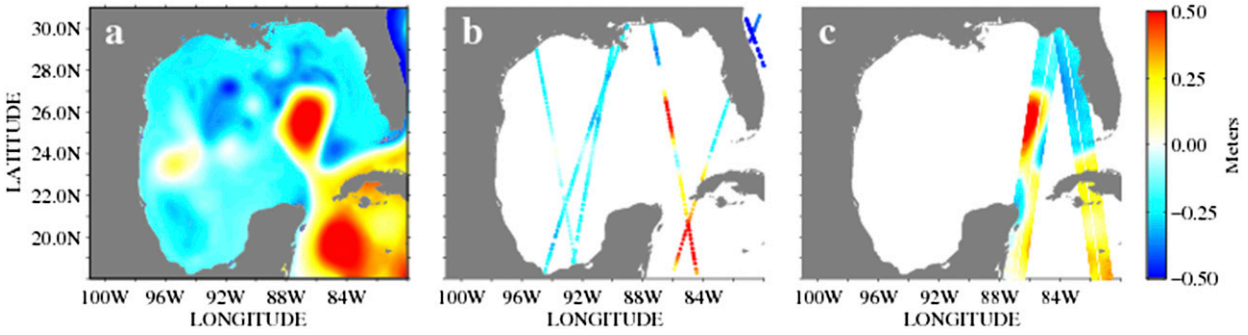

FIG. 3. Comparison of the (a) nature run, valid at 1 May 2014 to (b),(c) sampled conventional altimeter and SWOT observation from 1 to 2 May 2014, respectively.

profiling floats (Roemmich et al. 2001), expendable bathythermographs (XBT), and drifting buoys. SST observation locations are determined after applying superobservation averaging within NCODA and as such the nature run is sampled for SST observations at roughly 6-km resolution. The temperature and salinity profiles, on the other hand, are randomly distributed throughout the domain. Each of the assimilative experiments to be shown include these SST and subsurface temperature and salinity observations; the only difference in the experiments is in the source of the altimetry observations.

Altimeter observation positions are obtained from an array of orbiting satellites. These data are processed through the Altimeter Processing System (ALPS; Jacobs et al. 2002), which is available from the Altimetry Data Fusion Center (ADFC) at the Naval Oceanographic Office (NAVOCEANO). These processed observations include estimates of observation error that account for instrument and representation error, as is nominally provided by NCODA (Cummings 2005). For this twin-data assimilation experiment, the actual observed values are replaced, however, by linearly interpolating the nature run to the observed locations at the appropriate times. Like the SST data, this interpolation takes place after NCODA has applied superobservation averaging to the altimetry data and as such the along-track resolution is roughly equivalent to the model (i.e., 6 km). A Gaussian white noise is added to each simulated observation based on the observational instrument error amplitude provided by NCODA.

The simulated SWOT observations are provided via a PYTHON program suite made available by the SWOT science team, known as the SWOT Simulator (https://swot.jpl.nasa.gov/science/resources/). This program simulates the sea surface height observations that can be obtained by the SWOT instrument by sampling an ocean model solution using estimated information regarding satellite orbit characteristics as well as measurement error and noise (as described by the SWOT project team). This error comes from six expected sources: 1) Ka-band radar interferometer error, 2) roll error (due to movement of the satellite platform), 3) phase error, 4) timing error, 5) baseline dilatation error, and 6) wet troposphere error (caused by humidity in the atmosphere inducing a delay of the radar pulse). These errors are not uniform in space, but grow in magnitude toward the outer edge of the swath. The effect of the noise characteristics limits the SSH wavelength that can be accurately detected to around 20 km in the GoM domain (Fu and Ubelmann 2014). Figure 3 shows a comparison of simulated conventional altimeter tracks along with simulated SWOT observation for a 24-h period from 1 to 2 May 2014. Figure 3a shows the nature run on 1 May 2014, Fig. 3b shows the simulated conventional altimetry data, and Fig. 3c shows the simulated SWOT observations. It is immediately clear that the SWOT observations provide two-dimensional information in the cross- and along-track directions, whereas conventional altimeters only provide data in the along-track direction.

4. Twin-data assimilation experiment design and results

a. *Experiment design*

To fully assess the impact of SWOT-simulated observations in the assimilation, several experiments must be done. The first is the assimilation of all traditional observations including conventional altimeter observations; this experiment is hereafter referred to as ALT. The second experiment replaces the traditional altimeter observations with those from SWOT; this experiment is hereafter referred to as SWT. Finally, as in Pujol et al. (2012), a third experiment that combines SWOT with conventional altimeters is made; this is hereafter referred to as COM. The nonassimilative background run will be referred to as the "free run" or FR.

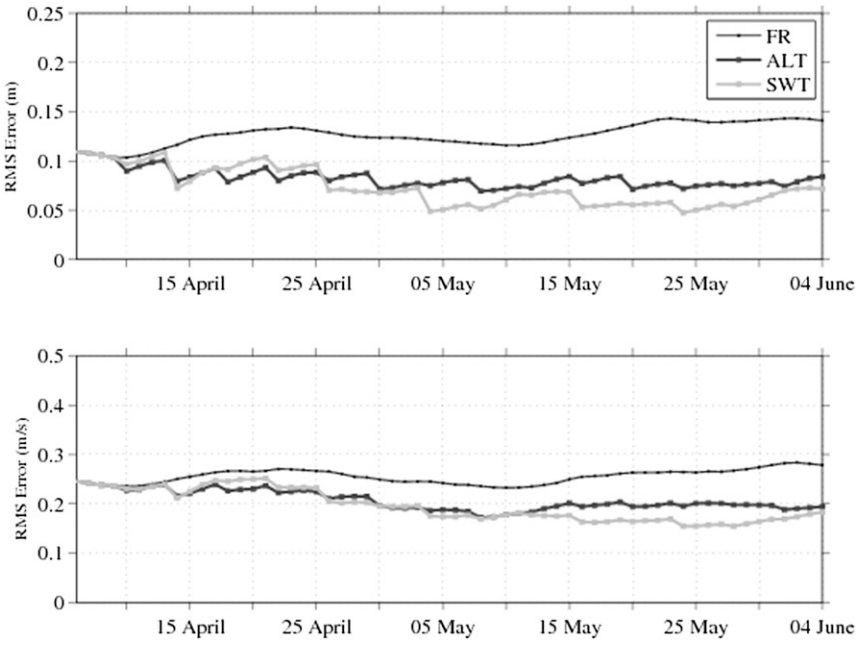

FIG. 4. Root-mean-square (RMS) error for (top) SSH and (bottom) velocity for the FR (thin black), ALT (thick black), and SWT (gray) experiments. RMS error of each experiment computed against nature run at all model points.

The process to assimilate the SWOT observations here is straightforward. Though it is expected that SWOT observation errors may be correlated along the satellite path due to platform roll error (Le Hénaff et al. 2008), no correlation between the observation errors is accounted for in the observation error covariance (it is assumed to be diagonal). In an attempt to account for this correlation, and also due to the length scale used in the background error covariance, the resolution of both the conventional altimeters and SWOT observations are degraded slightly. In the experiments shown here, the altimeter and SWOT observation densities are thinned in such a manner as to ensure that no two observations are within half a spatial correlation-scale distance (as defined in the static portion of the background error covariance employed by the NCOM-4DVAR). For this work the correlation scale is based on the Rossby radius of deformation, which for the Gulf of Mexico is roughly 40 km. Because of this, the examination here will be mainly focused on recovering mesoscale structures and surface currents. Other than thinning the altimeter observation density, no special treatment is used in the assimilation of the SSH observations. The procedure to assimilate these observations follows Ngodock et al. (2016) and Carrier et al. (2016). Finally, the initial condition and model errors used in the NCOM-4DVAR for this work follow Carrier et al. (2016); for the initial conditions, these errors are set to 0.2°C for temperature, 0.1 psu for salinity, $0.02\,\mathrm{m\,s^{-1}}$ for velocity; for the model error, the error is assumed to be within the surface atmospheric forcing and is roughly $40\,\mathrm{W\,m^{-2}}$ in surface heat flux and 0.25 Pa in surface wind stress.

Each experiment begins on 5 April, after a 4-day spinup period from the initial condition, and is run until 4 June 2014. Each experiment proceeds as a series of 96-h forecast/analysis windows, where at the end of each window the forecast model is run from the updated final analysis condition to provide the background forecast for the next 96-h window. Each 96-h forecast is compared to the nature run, at all model points, to assess the impact of the observation assimilation on the system.

b. *Experiment results and conclusions*

To get a general picture of the performance of the analysis–forecast experiments, each 96-h forecast from the ALT and SWT experiments is compared to the nature run at each model grid point by computing the time series of the root-mean-square (RMS) error over the entire experiment time period. The RMS error is computed as

$$\mathrm{RMS} = \sqrt{\frac{1}{M}\sum_{m=1}^{M}(x_m^t - x_m^b)^2}, \qquad (3)$$

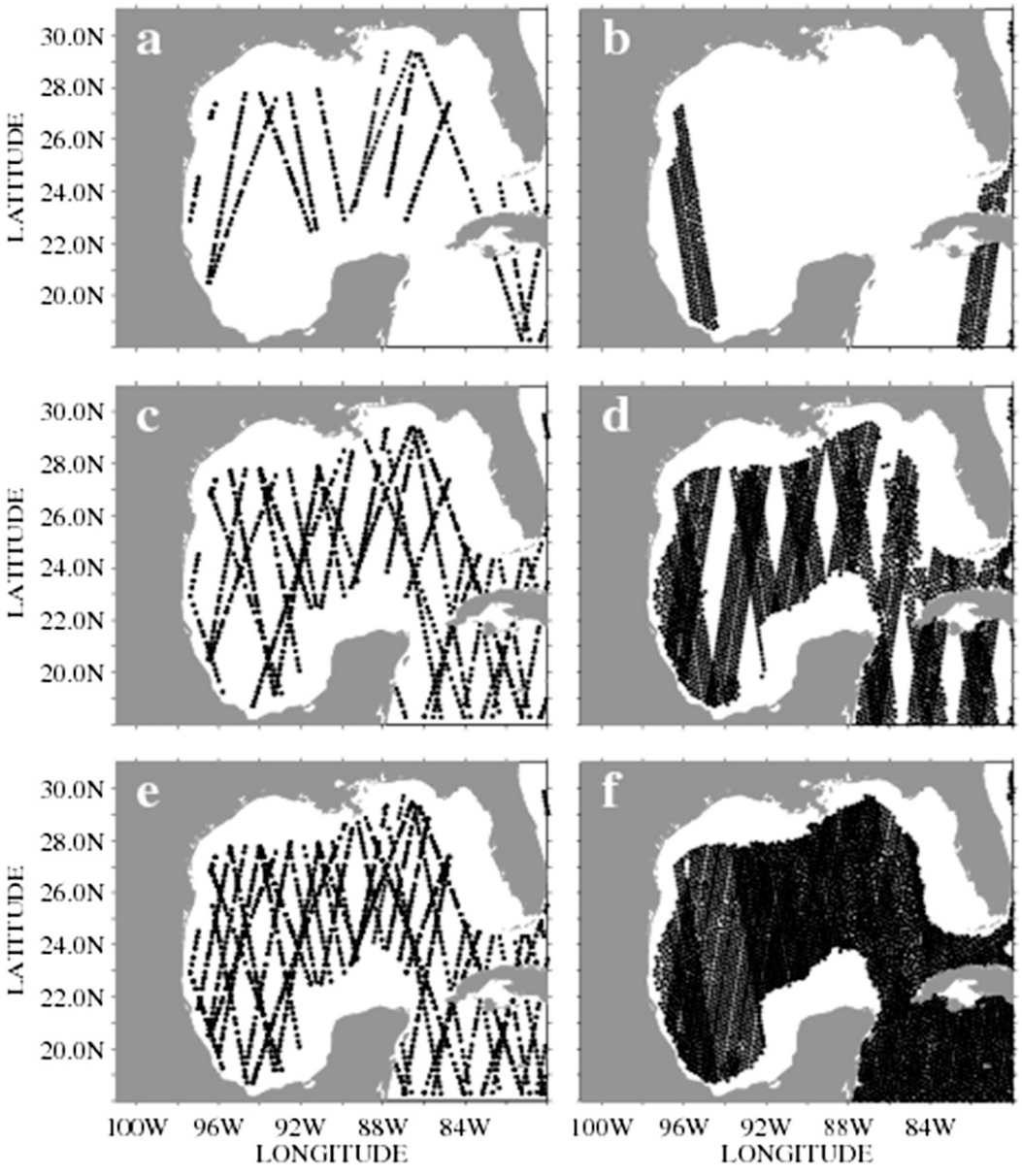

FIG. 5. Distribution of simulated satellite observations during 5–9 Apr 2014 for (a) conventional altimeters and (b) SWOT; accumulated during 5–17 Apr 2014 for (c) conventional altimeters and (d) SWOT; and accumulated during 5–25 Apr 2014 for (e) conventional altimeters and (f) SWOT.

where x_m^t is the mth model grid point of the nature run, x_m^b is the mth model grid point of the background run, and M is the size of the model state. Figure 4 shows the RMS error for the SSH field (top panel) and for the total velocity (bottom panel) for the FR (thin black), ALT (thick black), and SWT (gray) experiments. It is clear that both assimilation runs outperform the FR almost immediately in terms of both SSH and velocity, as the total RMS error for SSH, for both assimilative runs, falls to below 0.1 m by the end of the experiment; and below 0.2 m s^{-1} for velocity; FR stays near 0.15 m and 0.3 m s^{-1} for SSH and velocity, respectively. The fact that the FR error never generally decreases indicates that the free run model trajectory never approaches the nature run during the experiment time frame; therefore, any improvement seen in the assimilative model should be attributable to the assimilation of observations alone. It is interesting to note that the RMS error for both SSH and velocity is lower in the ALT experiment than in the SWT experiment before 25 April. After this date, the error in both fields from SWT becomes lower than that in ALT, indicating

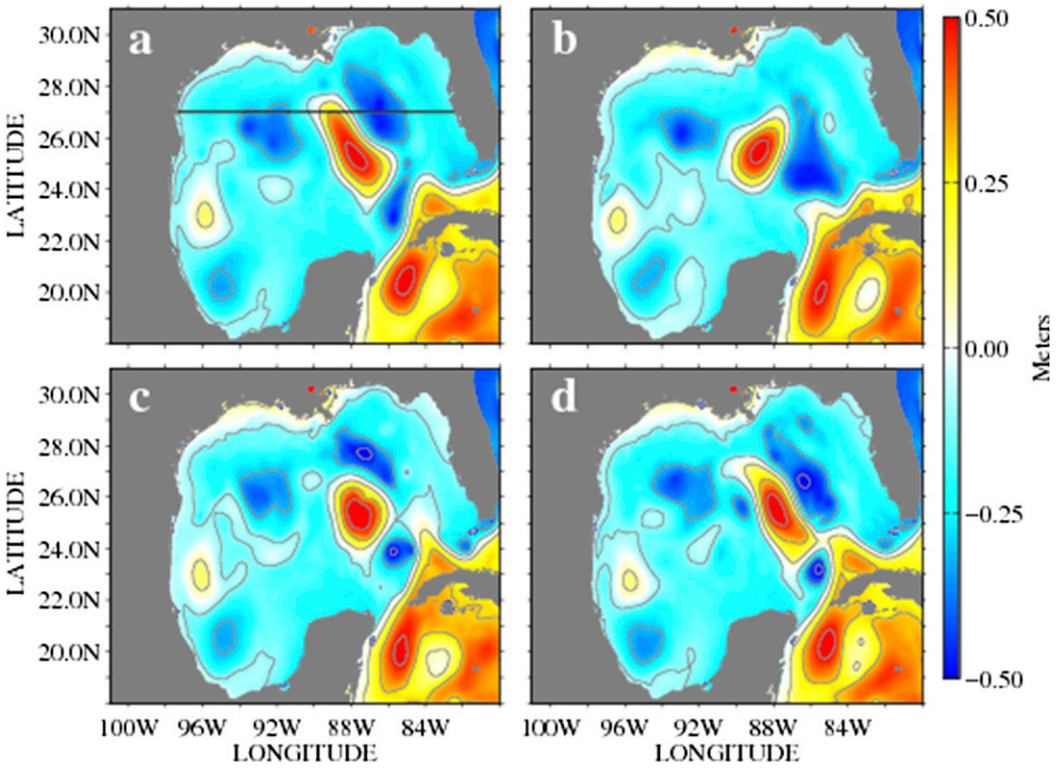

FIG. 6. Model SSH (m) valid for 4 Jun 2014: (a) nature run, (b) FR, (c) ALT, and (d) SWT experiments. The horizontal black line in (a) indicates the location of temperature cross section shown in Fig. 9.

that the assimilation of SWOT observations eventually produces a superior model state than from conventional altimeters. The fact that the SWT experiment does not immediately outperform the ALT experiment may be due to the distribution of observations throughout the domain in the initial stages of the experiment. The conventional altimeters have been simulated for multiple instruments (i.e., *Jason-2* and AltiKa) and, therefore, initially have more coverage of the GoM domain than the SWOT instrument alone. Figure 5 shows the distribution of simulated observations for conventional altimeters (Fig. 5a) and SWOT (Fig. 5b) from 5 to 9 April 2014; also shown is the accumulated coverage of conventional altimeters (Fig. 5c) and SWOT (Fig. 5d) from 5 to 17 April, and from 5 to 25 April (Figs. 5e and 5f). It is clear that, at least initially, the coverage of classical altimeters is more evenly distributed throughout the GoM domain than SWOT. However, by the end of the month of April, the altimeters, while exhibiting good coverage of the domain, possess coverage gaps in between satellite tracks; the SWOT observations, on the other hand, cover almost the entire domain.

Statistically, the SWT experiment appears to outperform ALT by the end of the experiment run; let us now examine the mesoscale eddy structure in the GoM from these experiments in comparison to the free and nature model runs. Figure 6 shows the model SSH on 4 June 2014 for the nature run (Fig. 6a), the free run (Fig. 6b), and the ALT (Fig. 6c) and SWT (Fig. 6d) experiments. At this time, the LCE in the nature run (Fig. 6a) is elongated in the northwest–southeast direction (centered near 25°N, 88°W) and is completely detached from the Loop Current. The Loop Current itself appears to be partially extended (near 24°N, 84°W) and there are cyclonic eddies to the east, west, and southeast of the LCE. The FR (Fig. 6b) solution shows a very different pattern, with a more circular LCE, no protrusion of the Loop Current into the GoM, and only two cyclonic eddies in the vicinity of the LCE (to the east and west). The ALT (Fig. 6c) run is a blend of the pattern seen in the nature and free runs. The primary LCE is more circular than what is seen in the nature run, but is just slightly more elongated in the northwest–southeast direction than the FR. The Loop Current, like the nature run, is slightly protruding into the southern GoM. Also, the ALT experiment exhibits the three cyclonic eddies surrounding the LCE, just as in the nature run, though with slightly different amplitudes and orientations. In

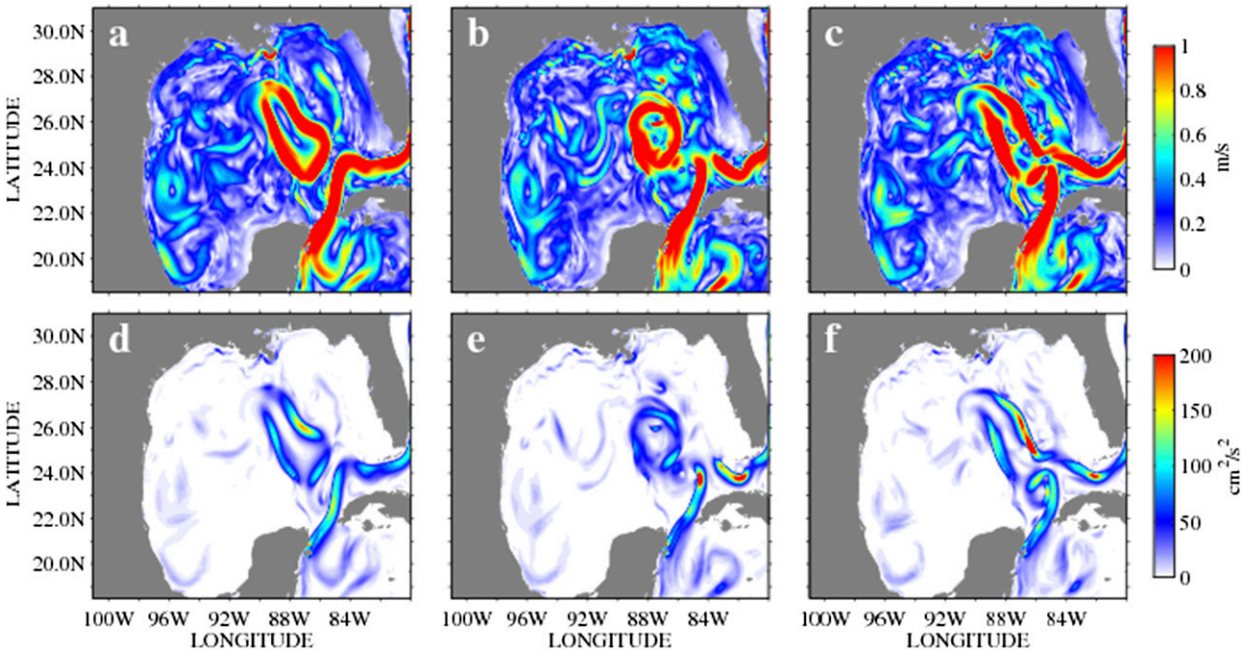

FIG. 7. Surface velocity magnitude for (a) the nature run, (b) the ALT experiment, and (c) the SWT experiment. (d)–(f) As in (a)–(c), but for surface eddy kinetic energy. Both fields shown for the 96-h forecast valid on 4 Jun 2014.

the Caribbean Sea, the ALT experiment exhibits a depression in the SSH (near 19.5°N, 83°W), which matches the FR, but not the nature run. The SWT (Fig. 6d) experiment, however, matches the nature run much closer than what is seen in the ALT experiment. The primary LCE is similar in shape and orientation to the nature run. The LCE is surrounded by three cyclonic eddies, as in the nature run; though, the cyclonic eddy to the south of the LCE is much smaller, resulting in the LCE in SWT being somewhat attached to the protrusion of the Loop Current into the southern GoM. Also, the SWT SSH field in the Caribbean Sea does not exhibit as large a depression near 19.5°N, 83°W as the ALT experiment, and this better matches the nature run. The improved match to the nature run in the SWT experiment can also be seen in the surface velocity and eddy kinetic energy fields as well. Figure 7 shows the surface velocity on 4 June 2014 for the nature run (Fig. 7a), ALT (Fig. 7b), and SWT (Fig. 7c) experiments; the eddy kinetic energy (EKE) field is shown for the nature run (Fig. 7d), ALT (Fig. 7e), and SWT (Fig. 7f) experiments. Examining the surface velocity, as indicated by the SSH field, the ALT experiment shows a more circular LCE than the nature run, though the location of the velocity ring associated with the LCE is similarly positioned as the

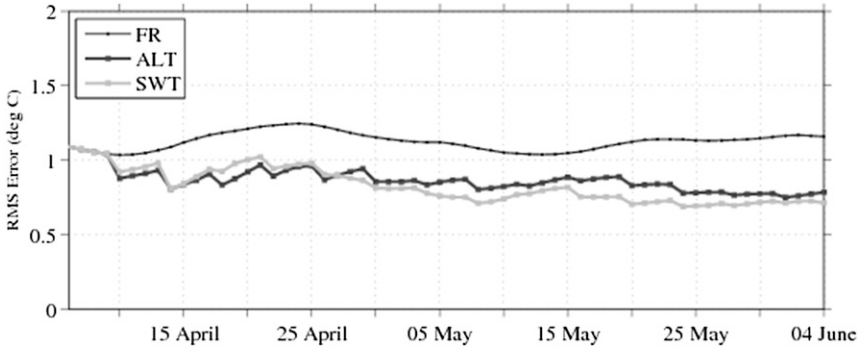

FIG. 8. Root-mean-square (RMS) error for temperature for the FR (thin black), ALT (thick black), and SWT (gray) experiments. RMS error of each experiment computed against nature run at all model points.

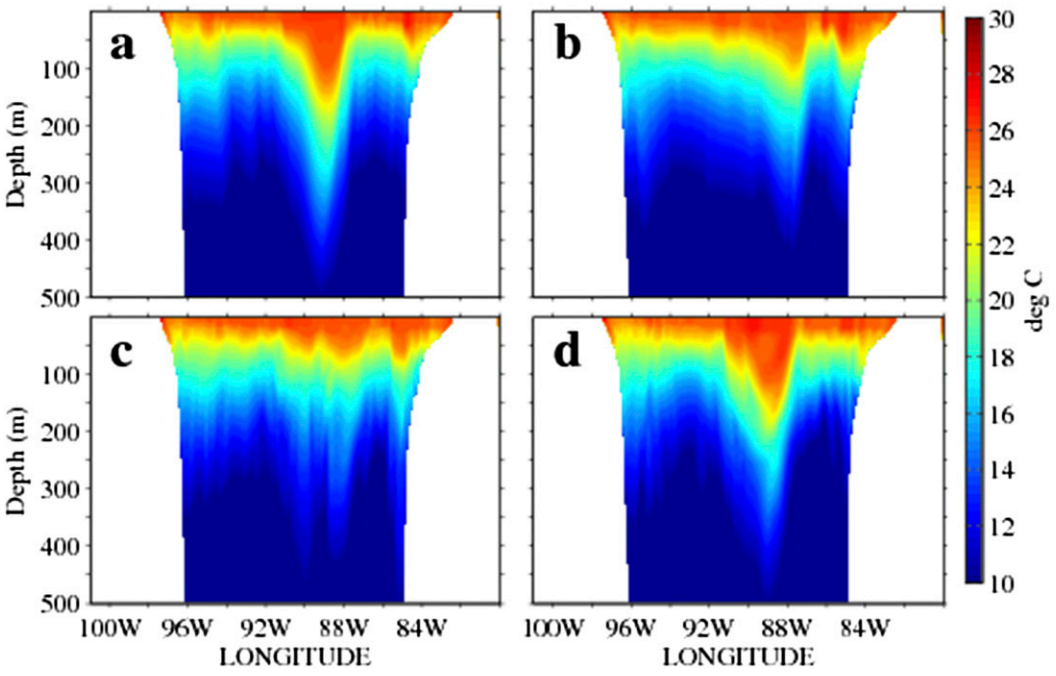

FIG. 9. Model temperature cross section (°C), valid on 4 Jun 2014, for (a) the nature run, (b) FR, (c) ALT, and (d) SWT experiments. The cross section is at latitude 27°N and runs east to west from 82° to 97°W.

nature run. The SWT experiment, on the other hand, has a surface velocity pattern that nearly matches the one seen in the nature run, albeit with a stronger entanglement with the Loop Current. Also, there appears to be submesoscale features near the center of the velocity ring associated with the LCE that are not present in the nature run. As for the EKE (Figs. 7d–f), which is calculated as

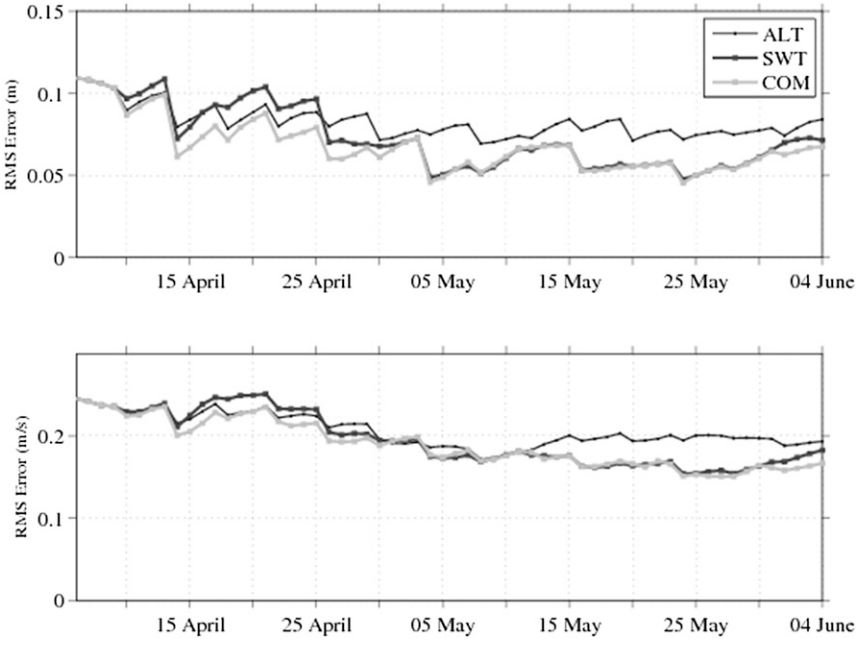

FIG. 10. RMS error for (top) SSH and (bottom) velocity for the ATL (thin black), SWT (thick black), and COM (gray) experiments. RMS error of each experiment computed against nature run at all model points.

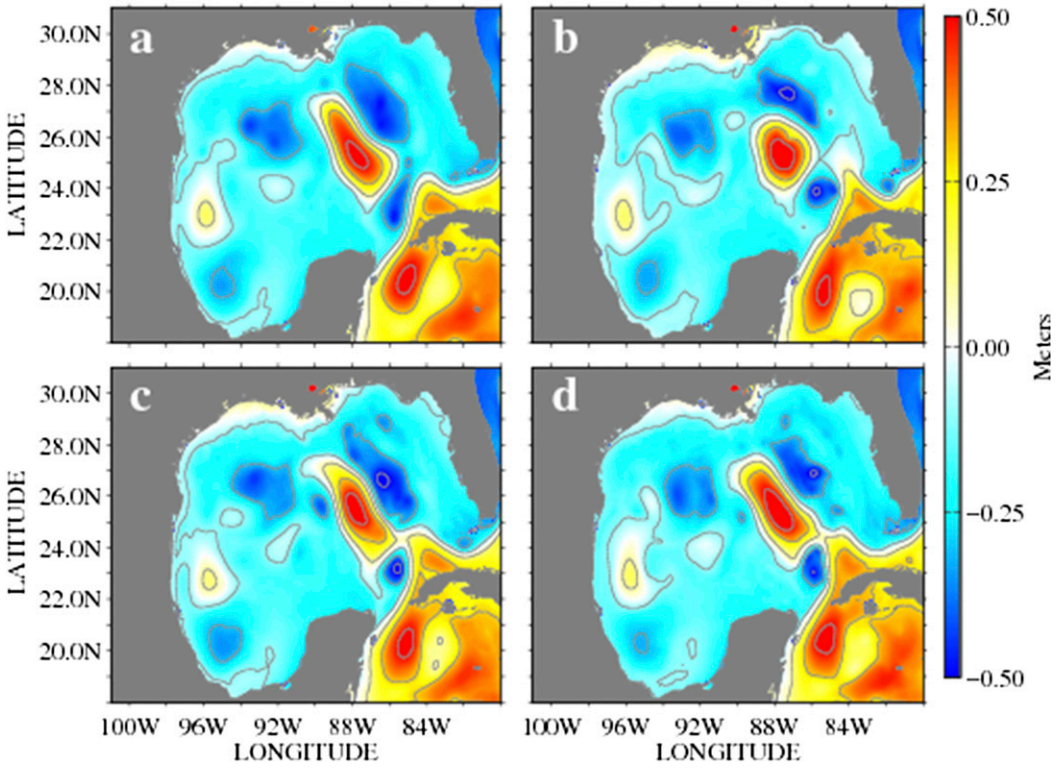

FIG. 11. Model SSH (m) valid on 4 Jun 2014, for (a) the nature run, (b) ALT, (c) SWT, and (d) COM experiments.

$$\mathrm{EKE} = \frac{1}{2}(u_*^2 + v_*^2), \tag{4}$$

where u_* and v_* are the zonal and meridional anomalies, respectively, from the mean geostrophic velocity components, it appears the energy in the vicinity of where the LCE is being shed from the LC is greater for both the ALT and SWT experiments than in the nature run. This may be a consequence of the fact that the LCE present in both the ALT and SWT experiments remain somewhat entangled with the LC; this is especially true for the SWT experiment. In both cases, the LCE is still in the process of being shed from the LC, whereas in the nature run, the LCE has completely shed from the LC and is progressing westward.

The mesoscale LCE also impacts the thermodynamic structure of the ocean subsurface in the vicinity of the eddy; therefore, any improvement in the surface mesoscale structure should extend to the ocean temperature as well. It should be noted that both ALT and SWT experiments assimilate the same simulated temperature observations; therefore, if one experiment exhibits superior performance in terms of the temperature fit to the nature run, it can be assumed that this difference is due to the type of altimeter observations used. Figure 8 shows the RMS error of the entire three-dimensional model temperature field, as compared to the nature run, for the FR (thin black), ALT (thick black), and SWT (gray) experiments. Like what is seen in Fig. 4, the SWT experiment's fit to the nature run temperature is not as good as the ALT experiment prior to 25 April. The SWT experiment temperature then outperforms that from the ALT experiment after this date, mirroring the behavior in the fit to the nature run SSH. As an example of the difference in the thermodynamic structure due to the LCE in ALT and SWT, we can examine a cross section of the model temperature in a region where the LCE structure is very different between the two assimilative forecasts. Figure 9 shows a cross section of the ocean model temperature (cross-sectional location displayed by thin black line in Fig. 6a) for the nature run (Fig. 9a), and the FR (Fig. 9b), ALT (Fig. 9c), and SWT (Fig. 9d) experiments, on 4 June 2014. This cross section is through the northernmost tip of the LCE, as seen in the nature run in Fig. 6a; the LCE does not extend that far north in the ALT experiment, though the SWT experiment does capture this structure well. The nature run temperature field exhibits a deep warm pool, associated with the elongated LCE, between 88° and 90°W that extends to almost 400 m; this pattern is not seen in the FR or ALT experiments. The SWT experiment captures this feature nicely in both meridional width as well as in depth. It is this difference, as well as other regions where

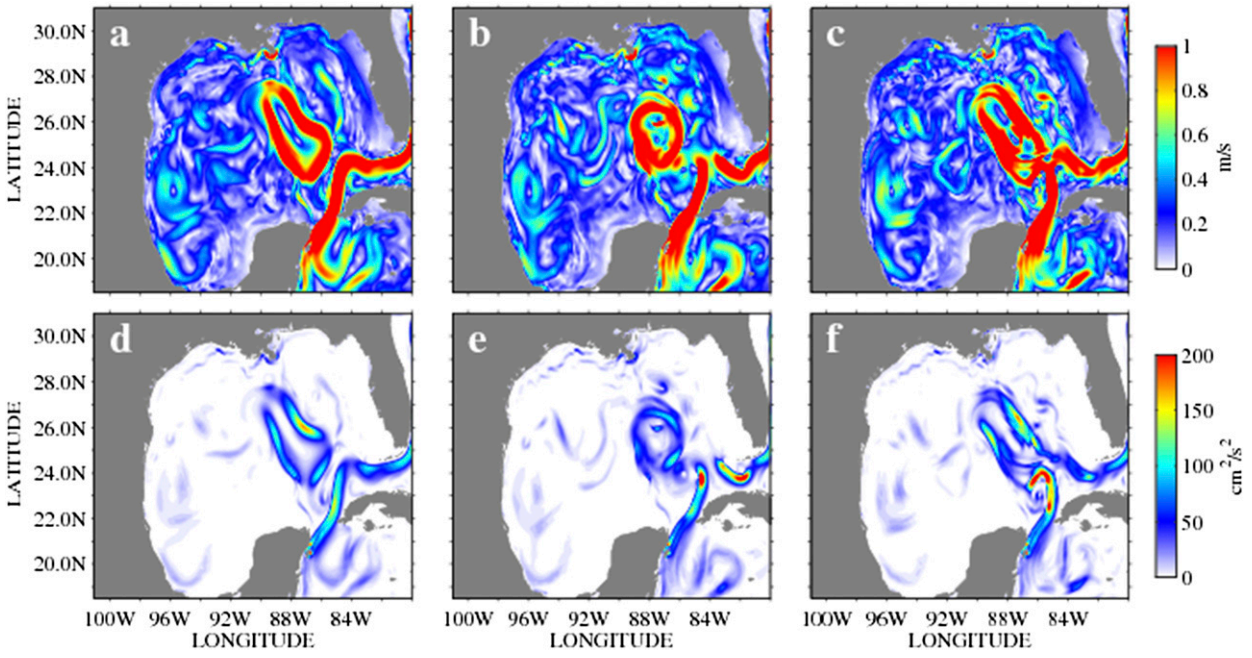

FIG. 12. Surface velocity magnitude for (a) the nature run, (b) the ALT experiment, and (c) the COM experiment. (d)–(f) As in (a)–(c), but for surface eddy kinetic energy. Both fields shown for the 96-h forecast are valid on 4 Jun 2014.

SWT is performing better than ALT, that is contributing to the improved temperature RMS error in Fig. 8.

It has been shown that the observations gathered from the SWOT instrument alone can, over time, help to improve the model surface mesoscale field to match the true state more closely than a suite of conventional altimeters. The obvious question is "What is the impact of combining these observations together?" Figure 10 shows the same time series RMS error plot as Fig. 4, but for the ALT (thin black), SWT (thick black), and the COM (gray) experiments. The COM experiment provides the best solution: the initial RMS error, prior to 25 April, is lower in COM than in either ALT or SWT. After that date, the error in the SWT and COM experiments appear to match quite well. This suggests that the additional coverage provided by the conventional altimeters helps to constrain the model SSH and velocity field in the early part of the experiment. However, from 25 April to 4 June, the added conventional altimeters do not appear to add more value than what is gained using SWOT observations alone. This is supported by the examination of the SSH fields on 4 June. Figure 11 shows the SSH field for the nature run (Fig. 11a), ALT (Fig. 11b), SWT (Fig. 11c), and COM (Fig. 11d) experiments. Similar to what is seen in Fig. 6d for SWT, the COM experiment is closer to the nature run than the ALT experiment, with the primary LCE elongated in the northwest–southeast direction. However, the shape of the LCE in COM is closer still to the nature run than that in SWT, particularly near the north and south edges of the LCE. Nevertheless, the COM experiment also shows the LCE somewhat associated with the protrusion of the Loop Current into the GoM, as was the case with SWT. The velocity fields at this time, seen in Fig. 12, show that COM (Fig. 12c) matches the nature run (Fig. 12a) better than ALT (Fig. 12b). The eddy kinetic energy analysis, shown in Figs. 12d–f, also indicates that the COM experiment (Fig. 12f) EKE pattern is closer in overall appearance to the nature run (Fig. 12d) than the ALT experiment (Fig. 12e). Though, as was seen in Fig. 7, the EKE near the entanglement of the LC and LCE in the COM experiment is higher than what is seen in the nature run. It does seem, however, that the addition of altimeter observations in the COM experiment has led to a slightly weaker LCE (in terms of the EKE), especially on the eastern side, than what is shown in the SWT experiment (Fig. 7f). The results shown in Figs. 11 and 12 indicate that with a long-enough training period, the assimilation of SWOT observations alone can help to improve the model SSH to match the true state better than conventional altimeters and nearly as well as a combination of SWOT and traditional altimeter observations.

5. Summary

The SWOT satellite is expected to provide SSHA observations within a wide swath with high spatial resolution. The impact of such data is investigated by way of twin-data assimilation experiments using the

NCOM-4DVAR data assimilation system. These experiments proceed as a series of 96-h assimilation windows, where the final condition of each window is used to initialize a 96-h forecast. It was shown here that the SWOT observations help to constrain the model mesoscale (50–250 km) and surface velocity throughout the 96-h forecast better than conventional altimeters alone. Based on these results, it appears that this improvement can be gained after correcting the model with observations for about one month. In addition to this, assimilating SWOT along with conventional altimeters only acts to improve the model representation of the mesoscale SSH and surface velocity in the early portion of the experiment, when the coverage of SWOT observations is limited to only a portion of the model domain. However, after assimilating SWOT observations for a longer period of time, the addition of conventional altimeter observations adds very little to the improvement of the model mesoscale representation. The results shown here suggest that the launch of even one satellite carrying the SWOT instrument will substantially improve the observational coverage of the ocean topography, which will result in a better model simulation of the ocean SSH and surface velocity through data assimilation. This improvement may be enhanced with additional satellites carrying wide-swath altimeters.

The resolution of the model used in this experiment is too coarse to investigate submesoscale features that may be observed with SWOT. Future efforts will investigate the use of SWOT observations in constraining and forecasting these features using a higher-resolution (~1 km) ocean model.

Acknowledgments. This work was sponsored by the Office of Naval Research under Grant N0001415WX00010.

REFERENCES

Barron, C. N., A. Birol Kara, H. E. Hurlburt, C. Rowley, and L. Smedstad, 2004: Sea surface height predictions from the global Navy Coastal Ocean Model during 1998–2001. *J. Atmos. Oceanic Technol.*, **21**, 1876–1893, doi:10.1175/JTECH-1680.1.

——, ——, P. J. Martin, R. C. Rhodes, and L. Smedstad, 2006: Formulation, implementation and examination of vertical coordinate choices in the Global Navy Coastal Ocean Model (NCOM). *Ocean Modell.*, **11**, 347–375, doi:10.1016/j.ocemod.2005.01.004.

——, ——, R. C. Rhodes, C. Rowley, and L. Smedstad, 2007: Validation test report for the 1/8° Global Navy Coastal Ocean Model Nowcast/Forecast System. NRL Rep. NRL/MR/7320-07-9019, 144 pp.

Bennett, A. F., 1992: *Inverse Methods in Physical Oceanography.* Cambridge University Press, 347 pp.

——, 2002: *Inverse Modeling of the Ocean and Atmosphere.* Cambridge University Press, 234 pp.

Bleck, R., 2002: An oceanic general circulation model framed in hybrid isopycnic-Cartesian coordinates. *Ocean Modell.*, **4**, 55–88, doi:10.1016/S1463-5003(01)00012-9.

Carrier, M. J., and H. Ngodock, 2010: Background-error correlation model based on the implicit solution of a diffusion equation. *Ocean Modell.*, **35**, 45–53, doi:10.1016/j.ocemod.2010.06.003.

——, ——, S. Smith, G. Jacobs, P. Muscarella, T. Ozgokmen, B. Haus, and B. Lipphardt, 2014: Impact of assimilating ocean velocity observations inferred from Lagrangian drifter data using the NCOM-4DVAR. *Mon. Wea. Rev.*, **142**, 1509–1524, doi:10.1175/MWR-D-13-00236.1.

——, ——, P. Muscarella, and S. Smith, 2016: Impact of assimilating surface velocity observations on the model sea surface height using the NCOM-4DVAR. *Mon. Wea. Rev.*, **144**, 1051–1068, doi:10.1175/MWR-D-14-00285.1.

Chua, B. S., and A. F. Bennett, 2001: An inverse ocean modeling system. *Ocean Modell.*, **3**, 137–165, doi:10.1016/S1463-5003(01)00006-3.

Coelho, E. F., and Coauthors, 2015: Ocean current estimation using a multi-model ensemble Kalman filter during the Grand Lagrangian Deployment experiment (GLAD). *Ocean Modell.*, **87**, 86–106, doi:10.1016/j.ocemod.2014.11.001.

Cooper, C., G. Z. Forristall, and T. M. Joyce, 1990: Velocity and hydrographic structure of two Gulf of Mexico warm-core rings. *J. Geophys. Res.*, **95**, 1663–1679, doi:10.1029/JC095iC02p01663.

Cummings, J. A., 2005: Operational multivariate ocean data assimilation. *Quart. J. Roy. Meteor. Soc.*, **131**, 3583–3604, doi:10.1256/qj.05.105.

——, and O. M. Smedstad, 2013: Variational data assimilation for the global ocean. *Data Assimilation for Atmospheric, Oceanic and Hydrologic Applications, Vol. II*, S. K. Park and L. Xu, Eds., Springer-Verlag, 303–343, doi:10.1007/978-3-642-35088-7_13.

Fu, L.-L., and C. Ubelmann, 2014: On the transition from profile altimeter to swath altimeter for observing global ocean surface topography. *J. Atmos. Oceanic Technol.*, **31**, 560–568, doi:10.1175/JTECH-D-13-00109.1.

Halliwell, G. R., A. Srinivasan, V. H. Kourafalou, H. Yang, D. Willey, M. Le Henaff, and R. Atlas, 2014: Rigorous evaluation of a fraternal twin ocean OSSE system for the Open Gulf of Mexico. *J. Atmos. Oceanic Technol.*, **31**, 105–130, doi:10.1175/JTECH-D-13-00011.1.

Jacobs, G. A., C. N. Barron, D. N. Fox, K. R. Whitmer, S. Klingenberger, D. May, and J. P. Blaha, 2002: Operational altimeter sea level products. *Oceanography*, **15**, 13–21, doi:10.5670/oceanog.2002.32.

——, and Coauthors, 2014: Data assimilation considerations for improved ocean predictability during the Gulf of Mexico Grand Lagrangian Deployment (GLAD). *Ocean Modell.*, **83**, 98–117, doi:10.1016/j.ocemod.2014.09.003.

Le Hénaff, M., P. De Mey, B. Mourre, and P.-Y. Le Traon, 2008: Contribution of a wide-swath altimeter in a shelf seas assimilation system: Impact of the satellite roll errors. *J. Atmos. Oceanic Technol.*, **25**, 2133–2144, doi:10.1175/2008JTECHO576.1.

Le Traon, P. Y., P. Klein, B. L. Hua, and G. Dibarboure, 2008: Do altimeter wavenumber spectra agree with the interior or surface quasigeostrophic theory? *J. Phys. Oceanogr.*, **38**, 1137–1142, doi:10.1175/2007JPO3806.1.

Leben, R., 2005: Altimeter-derived loop current metrics. *Circulation in the Gulf of Mexico: Observations and Models, Geophys.*

Monogr., Vol. 161, Amer. Geophys. Union, 181–201, doi:10.1029/161GM15.

Lillibridge, J., R. Scharro, S. Abdalla, and D. Vandemark, 2014: One- and two-dimensional wind speed models for Ka-band altimetry. *J. Atmos. Oceanic Technol.*, **31**, 630–638, doi:10.1175/JTECH-D-13-00167.1.

Martin, P. J., and Coauthors, 2009: User's manual for the Navy Coastal Ocean Model (NCOM) version 4.0. NRL Rep. NRL/MR/7320-09-9151, 68 pp.

Mellor, G. L., and T. Yamada, 1982: Development of a turbulence closure model for geophysical fluid problems. *Rev. Geophys. Space Phys.*, **20**, 851–875, doi:10.1029/RG020i004p00851.

Muscarella, P., M. J. Carrier, H. Ngodock, S. Smith, B. L. Lipphardt, A. D. Kirwan Jr., and H. S. Huntley, 2015: Do assimilated drifter velocities improve Lagrangian predictability in an operational ocean model? *Mon. Wea. Rev.*, **143**, 1822–1832, doi:10.1175/MWR-D-14-00164.1.

Ngodock, H. E., and M. J. Carrier, 2013: A weak constraint 4D-Var assimilation system for the Navy Coastal Ocean Model using the representer method. *Data Assimilation for Atmospheric, Oceanic and Hydrologic Applications*, *Vol. II*, S. K. Park and L. Xu, Eds., Springer-Verlag, 367–390, doi:10.1007/978-3-642-35088-7_15.

——, and ——, 2014: A 4DVAR system for the Navy Coastal Ocean Model. Part I: System description and assimilation of synthetic observations in the Monterey Bay. *Mon. Wea. Rev.*, **142**, 2085–2107, doi:10.1175/MWR-D-13-00221.1.

——, ——, I. Souopgui, S. R. Smith, P. Martin, P. Muscarella, and G. Jacobs, 2016: On the direct assimilation of along-track sea surface height observations into a free-surface ocean model using a weak constraints four dimensional variational (4D-Var) method. *Quart. J. Roy. Meteor. Soc.*, **142**, 1160–1170, doi:10.1002/qj.2721.

Ochoa, J., J. Sheinbaum, A. Badan, J. Candela, and D. Wilson, 2001: Geostrophy via potential vorticity inversion in the Yucatan Channel. *J. Mar. Res.*, **59**, 725–747, doi:10.1357/002224001762674917.

Oey, L., T. Ezer, and H. Lee, 2005: Loop current, rings, and related circulation in the Gulf of Mexico: A review of numerical models and future challenges. *Circulation in the Gulf of Mexico: Observations and Models, Geophys. Monogr.*, Vol. 161, Amer. Geophys. Union 161, 31–56, doi:10.1029/161GM04.

Pujol, M.-L., G. Dibarboure, P.-Y. Le Traon, and P. Klein, 2012: Using high-resolution altimetry to observe mesoscale signals. *J. Atmos. Oceanic Technol.*, **29**, 1409–1416, doi:10.1175/JTECH-D-12-00032.1.

Richman, J. G., B. K. Arbic, J. F. Shriver, E. J. Metzger, and A. J. Wallcraft, 2012: Inferring dynamics from the wavenumber spectra of an eddying global ocean model with embedded tides. *J. Geophys. Res.*, **117**, C12012, doi:10.1029/2012JC008364.

Roemmich, D., and Coauthors, 2001: Argo: The global array of profiling floats. *Observing the Oceans in the 21st Century*, C. J. Koblinsky and N. R. Smith, Eds., Melbourne Bureau of Meteorology, 248–257.

Sasaki, H., and P. Klein, 2012: SSH wavenumber spectra in the North Pacific from a high-resolution realistic simulation. *J. Phys. Oceanogr.*, **42**, 1233–1241, doi:10.1175/JPO-D-11-0180.1.

Schlitz, R. J., 1973: Net total transport and net transport by water mass categories for Yucatan Channel, based on data for April 1970. Ph.D. dissertation, Texas A&M University, 106 pp.

Smagorinsky, J., 1963: General circulation experiments with the primitive equations. I: The basic experiment. *Mon. Wea. Rev.*, **91**, 99–164, doi:10.1175/1520-0493(1963)091<0099:GCEWTP>2.3.CO;2.

Ubelmann, C., P. Klein, and L.-L. Fu, 2015: Dynamic interpolation of sea surface height and potential applications for future high-resolution altimetry mapping. *J. Atmos. Oceanic Technol.*, **32**, 177–184, doi:10.1175/JTECH-D-14-00152.1.

Weaver, A. T., and P. Courtier, 2001: Correlation modeling on the sphere using a generalized diffusion equation. *Quart. J. Roy. Meteor. Soc.*, **127**, 1815–1846, doi:10.1002/qj.49712757518.